(Scientific Note)

# Material Processing of Convection-Driven Flow Field and Temperature Distribution Under Oblique Gravity

RU J. HUNG AND YING-TIAN LONG

*Department of Mechanical Aerospace Engineering*
*The University of Alabama in Huntsville*
*Huntsville, Alabama, U.S.A.*

## ABSTRACT

A set of mathematical formulations is adopted to study vapor deposition from source materials driven by a heat transfer process under normal and oblique directions of gravitational acceleration with an extremely low pressure environment of $10^{-2}$ mmHg. A time step animation series of the initiation and development of flow and temperature profiles during the course of vapor deposition has been obtained through the numerical computation. Computations show that the process of vapor deposition is accomplished by the transfer of vapor though a fairly complicated flow pattern of recirculation under normal direction gravitational acceleration. It is obvious that there is no way to produce a homogeneous thin crystalline film with fine grains under such a complicated flow pattern of recirculation with a non-uniform temperature distribution under normal direction gravitational acceleration. There is no vapor deposition due to a stably stratified medium without convection for reverse normal direction gravitational acceleration. Vapor deposition under oblique direction gravitational acceleration in the vertial direction is favorable for production of a homogeneous thin crystalline film. However, oblique direction gravitational acceleration also induces an unfavorable gravitational acceleration along the horizontal direction, which is responsible for initiation of a complicated flow pattern of recirculation. In other words, it will be necessary to carry out vapor deposition under a reduced gravity in future space shuttle experiments with an extremely low pressure environment so as to process vapor deposition with a homogeneous crystalline film with fine grains. Fluid mechanics simulation can be used as a tool to suggest the most optimistic experimental method with the best setup to achieve the goal of processing the best nonlinear optical materials.

**Key Words:** material processing, convection driven flow, flow field, temperature distribution

## I. Introduction

In recent years, a great deal of interest has been directed toward the use of organic materials in the development of higher efficiency optoelectronic devices. There is a myriad of possibilities among organics, which allows flexibility in the design of unique structures with a variety of functional group objectives. The use of nonlinear optical (NLO) organic materials as thin film waveguides allows full exploitation of their desirable qualities by permitting long interaction lengths and large power densities with modest power input (Nayar and Winter, 1990). There are several methods in use for preparing thin films such as the Langmuir-Blodgett method (Carter *et al.*, 1983; Kajzar *et al.*, 1983; Kajzar and Meissier, 1988), growth from sheared solution or melt (Thakur and Meyler, 1985; Thakur

*et al.*, 1986; Seymour *et al.*, 1985), and melt growth between glass plates (Ledoux *et al.*, 1986). This method for preparing thin films has shown some evidence that microgravity processing with extremely low pressure of $10^{-2}$ mm Hg may be beneficial (Paley *et al.*, 1992).

Epitaxial growth on ordered organic and inorganic substrates and variations in processing conditions have been used to prepare highly oriented polydiacetylene and phthalocyanine films (Paley *et al.*, 1992). The relationships of processing conditions to uniformity in thickness, the degree of orientation, and nonlinear optical properties are very important. Also, improvements in fabrication techniques for growth of thin films by means of vapor deposition would be useful. Time variation of the initiation and formulation of flow fields and temperature distributions during the vapor deposition process under an

extremely low pressure environment (Paley *et al.*, 1992) can provide a better understanding of the framework to determine whether nonlinear optical thin films should be grown in space to improve uniformity in thickness and homogeneity if ground-based research and theoretical studies indicate that this is feasible.

The NASA Marshall Space Flight Center is currently performing research to vapor deposit films of phthalocyanine and diacetylene monomer (Paley *et al.*, 1992). A better understanding of flow profiles and temperature distribution for vapor, which is produced from source material and propagates through the major driving mechanisms of heat transfer with natural convection and diffusion processes, can greatly enhance and improve the technique of nonlinear optical material processing.

In this study, the initiation and development of time-dependent, three-dimensional fluctuations of flow profiles and temperature distribution driven by heat transfer with natural convection under normal and oblique directions of gravitational acceleration with an extremely low pressure environment have been considered (Paley *et al.*, 1992). The purpose of this study was to investigate the possibility of processing vapor deposition under normal gravity with various directions to produce a homogeneous thin crystalline film with fine grains. Results of the present study will provide the critical guidelines for future space shuttle experiments. The size of the container adopted in this simulation will serve directly to facilitate the infrastructures to be used for both ground-based and space shuttle experiments.

## II. Mathematical Formulation

The governing equations, and the initial and boundary conditions for the present study of convection-driven material processing are illustrated below.

### 1. Governing Equations

Consider a co-axial cylinder with an inner radius of $R_1$ and an outer radius of $R_2$. The heights of the outer and inner cylinders are $L_2$ and $(L_2-L_1)$, respectively. Figure 1 shows the geometrical configuration of the co-axial ʻcylinder. For the purpose of considering the mathematical formulation, we adopt cylindrical coordinates $(r, \theta, z)$ with corresponding velocity components $(u, v, w)$ and corresponding components of gravity acceleration

$(g_r, g_\theta, g_z)$. Figure 1(a) and (b) show the geometrical configuration of a co-axial cylinder in the $r-z$ plane and $r-\theta$ plane, respectively. There are two temperature zones in this co-axial cylinder. The external walls of the outer cylinder are surrounded by a water jacket which maintains a constant temperature of 120°C while the walls of the inner cylinder keep a constant temperature of 30°C. The cell, containing air, is evacuated to a pressure of $10^{-2}$ mmH$_g$ ($=1.333$ N/m$^2$), and the gap between the outer and inner walls of the co-axial cylinder is filled. The flow profiles and temperature distributions of low pressure air are mainly governed by the natural convection of the flow pattern in this prob-
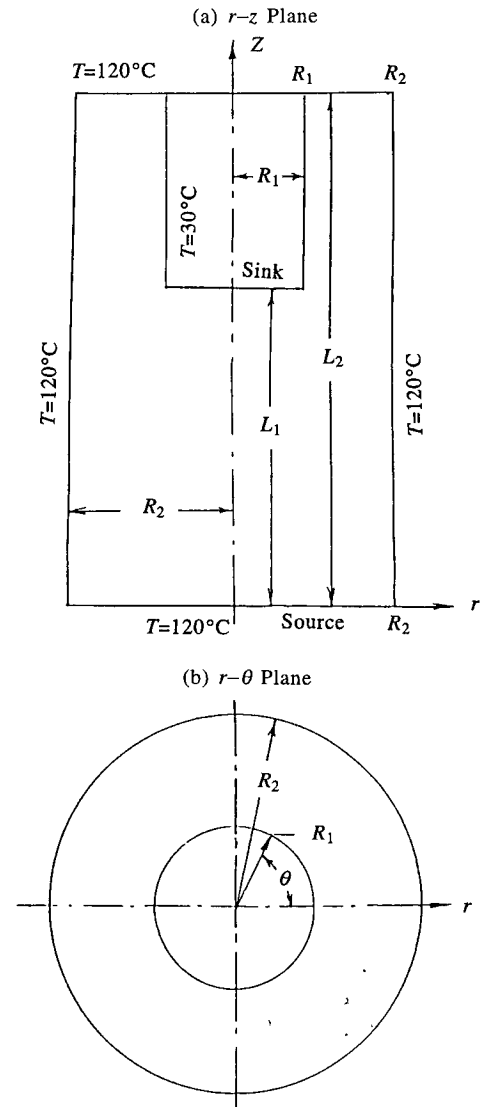


Fig. 1. Geometrical illustration of co-axial cylinders to be used for mathematical modeling, (a) in the $r-z$ plane, and (b) in the $r-\theta$ plane.

lem. The governing equations can be shown as follows:

(1) Continuity Equation

$$\frac{1}{r}\frac{\partial}{\partial r}(ru) + \frac{1}{r}\frac{\partial v}{\partial \theta} + \frac{\partial w}{\partial z} = 0 . \tag{1}$$

(2) Momentum Equations

$$\rho\left(\frac{\partial u}{\partial t} + u\frac{\partial u}{\partial r} + \frac{v}{r}\frac{\partial u}{\partial \theta} - \frac{v^2}{r} + w\frac{\partial u}{\partial z}\right)$$

$$= -\frac{\partial p}{\partial r} - \rho g_x[1 - \beta(T - T_\infty)] + \mu(\nabla^2 u - \frac{u}{r^2} - \frac{2}{r^2}\frac{\partial v}{\partial \theta}) \tag{2}$$

$$\rho\left(\frac{\partial v}{\partial t} + u\frac{\partial v}{\partial r} + \frac{v}{r}\frac{\partial v}{\partial \theta} + \frac{uv}{r} + w\frac{\partial v}{\partial z}\right)$$

$$= -\frac{1}{r}\frac{\partial p}{\partial \theta} - \rho g_\theta[1 - \beta(T - T_\infty)] + \mu(\nabla^2 v - \frac{v}{r^2} + \frac{2}{r^2}\frac{\partial u}{\partial \theta}) \tag{3}$$

$$\rho\left(\frac{\partial w}{\partial t} + u\frac{\partial w}{\partial r} + \frac{v}{r}\frac{\partial w}{\partial \theta} + w\frac{\partial w}{\partial z}\right)$$

$$= -\frac{\partial p}{\partial z} - \rho g_z[1 - \beta(T - T_\infty)] + \mu\nabla^2 w , \tag{4}$$

where

$$\beta = -\frac{1}{\rho_\infty}\left(\frac{\partial \rho}{\partial T}\right)_p , \quad \nabla^2 = \frac{1}{r}\frac{\partial}{\partial r}(r\frac{\partial}{\partial r}) + \frac{1}{r^2}\frac{\partial^2}{\partial \theta^2} + \frac{\partial^2}{\partial z^2}$$

and

$$(g_r, g_\theta, g_z) = g(\sin\psi\cos\theta, -\sin\psi\sin\theta, -\cos\psi).$$

(3) Energy Equation

$$\rho c_p\left(\frac{\partial T}{\partial t} + u\frac{\partial T}{\partial r} + \frac{v}{r}\frac{\partial T}{\partial \theta} + w\frac{\partial T}{\partial z}\right) = k\nabla^2 T . \tag{5}$$

Here, $\rho$, $p$, $T$, $\mu$, $k$, and $g$ denote the density, pressure, temperature, viscous coefficient, heat conduction coefficient of air, and background gravity acceleration, respectively. $\psi$ is the angle between the gravity vector and the axis of the cylinder. In this case, $T_\infty$ and $\rho_\infty$ represent the air temperature and density at $10^{-2}$ mmHg and the heat sink at the wall of the inner cylinder at $T=30°C$. In these mathematical expressions, the Boussinesq approximation is employed to formulate the relationship between local fluctuations of density and temperature through the thermal expansion coefficient $\beta$, with replaces the equation of state.

## 2. Initial and Boundary Conditions

The initial and boundary conditions have been assigned explicitly to solve governing Eqs. (1) to (5) simultaneousl.

### A. Initial Condition

At time $t=0$, all the flow profiles vanish, i.e.

$$u=v=w=0 \text{ everywhere.} \tag{6}$$

The temperature distribution of fluid along the inner cylinder is 30°C, and that of the water jacket surrounding the outer cylinder is 120°C, which is expressed by

$$T=30°C \quad \text{at } r \leq R_1, \ 0 \leq \theta \leq 2\pi, \quad L_1 \leq z \leq L_2 \tag{7}$$

$$T=120°C \text{ at } z=0; \ r \geq 0; \ 0 \leq \theta \leq 2\pi \tag{8}$$

$$\text{at } z=L_2; \ r \geq 0; \ 0 \leq \theta \leq 2\pi \tag{9}$$

$$\text{at } 0 \leq z \leq L_2; \ r=R_2; \ 0 \leq \theta \leq 2\pi. \tag{10}$$

The pressure profile inside the container is

$$p=10^{-2} \text{ mmHg} = 1.333 \text{ N/m}^2. \tag{11}$$

### B. Boundary Conditions

At time $t>0$, the temperature distribution shown in Eqs. (7) to (10), and the pressure profile shown in Eq. (11) remain true.

For the flow profiles, no penetration and no slip coditions along the surfaces of solid walls shall apply, namely

$$u=v=w=0 \tag{12}$$

along the surfaces of

$$r=R_1, \ 0 \leq \theta \leq 2\pi, \ L_1 \leq z \leq L_2; \tag{13}$$

$$r \geq 0, \ 0 \leq \theta \leq 2\pi, \ z=0; \tag{14}$$

$$r \geq 0, \ 0 \leq \theta \leq 2\pi, \ z=L_2; \tag{15}$$

and

$$r=R_2, \ 0 \leq \theta \leq 2\pi, \ 0 \leq z \leq L_2. \tag{16}$$

A co-axial cylindrical container designed to be used directly in future space shuttle experiments is illustrated in Fig. 1 with the following specifications: $L_1=6$ cm, $L_2=12$ cm, $R_1=0.9$ cm, and $R_2=1.5$

cm. The physical parameters for determining flow fields and temperature distributions are: gravity acceleration $g_o$=9.81 m/s$^2$, air pressure=1.333 N/m$^2$, air density=1.71×10$^{-5}$ kg/m$^3$, air viscosity coefficient =2.0×10$^{-5}$ m$^2$/s, coefficient of thermal expansion for air ($\beta$)=2.87×10$^{-3}$ L/K, and Prandtl number for air= 0.72.

To investigate the most significant driving parameters in this study, let us consider the inertia, buoyancy and viscous terms,

$$\omega \cdot \omega / L \sim g_z \beta \Delta T \sim v \omega / \delta_T^2, \tag{17}$$

respectively, which are on the same order of magnitude in the momentum equation shown in Eq. (4); and the convection and conduction terms,

$$\omega / L \Delta T \sim \alpha \ \Delta T / \delta_T^2, \tag{18}$$

respectively, which are also on the same order of magnitude in the energy equation shown in Eq. (5). Here, $\delta_T$ is the thermal boundary layer thickness; $L$ is the height of the container along the $z$-axis; $v=\mu/\rho$ is the kinematic viscosity; and $\alpha=k/\rho c_p$ is the thermal diffusivity. From convection and conduction terms in Eq. (18), from inertia and buoyancy terms in Eq. (17); and from buoyancy and viscous terms in Eq. (17), we can obtain the induced convective velocity of flows as follows:

$$\omega \sim \alpha L / \delta_T^2 \tag{19}$$

$$\omega \sim (g_z \beta L \Delta T)^{1/2} \tag{20}$$

and

$$w \sim (g_z \beta \delta_T^2 \Delta T) / v, \tag{21}$$

respectively. By equating Eqs. (19) and (21), we have the relationship

$$\delta_T / L \sim Ra^{-1/4}, \tag{22}$$

based on the balance between buoyancy and viscous forces. By equating Eqs. (19) and (20), we have another relationship:

$$\delta_T / L \sim (Ra \cdot Pr)^{-1/4} \sim (Gr)^{-1/4} (Pr)^{-1/2}, \tag{23}$$

based on the balance between buoyancy and inertia forces. Here, the Rayleigh number $(Ra)$, Grashof number $(Gr)$, and Prandtl number $(Pr)$ are defined as

$$Ra = g_z \beta L^3 \Delta T / \alpha v \tag{24}$$

$$Gr = g_z \beta L^3 \Delta T / v^2 = Ra / Pr \tag{25}$$

and

$$Pr = v / \alpha. \tag{26}$$

Since the heat transfer coefficient scales as $k/\delta_T$ (Bejan, 1995), the Nusselt number $(Nu)$ varies as

$$Nu = hL/K \sim Ra^{1/4} \tag{27}$$

from Eq. (22) based on the balance between buoyancy and viscous forces inside the thermal layer; and $Nu$ varies as

$$Nu \sim (Ra \cdot Pr)^{1/4} \sim (Gr)^{1/4} (Pr)^{1/2} \tag{28}$$

from Eq. (23) based on the balance between inertia and buoyancy forces inside the thermal layer. As indicated by Bejan (1995), both theoretical and laboratory measurements show that Eq. (27) is particularly applicable for $Pr>1$ fluids while Eq. (28) is dominated by $Pr<<1$ fluids. For the case of the present research, the dominant parameter is the Rayleigh number rather than the Grashof number (Bejan, 1995).

In this study, it will be shown later in the numerical simulation that the maximum induced flow velocity driven by convection is 0.2 m/s. The Reynolds number $(Re=\omega D/v$, where $D$ is the diameter of the container) for the flow pattern based on this maximum flow velocity is 150, which is far below the threshhold for production of turbulent flow fields. The Grashof $(Gr)$ and Rayleigh $(Ra)$ numbers for the present case study are 8×10$^6$ and 7.8×10$^6$, respectively, under the normal gravity conditions. It is well-known that the condition for the onset of convection with fluid layers heated from below is $Ra>1.1\times10^3$ (Bejan, 1995). In other words, the total elimination of the onset of induced convection, considering the proposed container size, is possible only in a reduced gravity environment of 10$^{-4}$ $g_o$ and below.

## III. Mathematical Simulation of Flow Profiles and Temperature Distributions

Equations (1) to (5) subject to the initial conditions shown in Eqs. (8) to (11) and the boundary conditions shown in Eqs. (12) to (16) have been used to solve time-dependent, three-dimensional flow profiles and temperature distributions numerically. The computer algorithms employed in this study
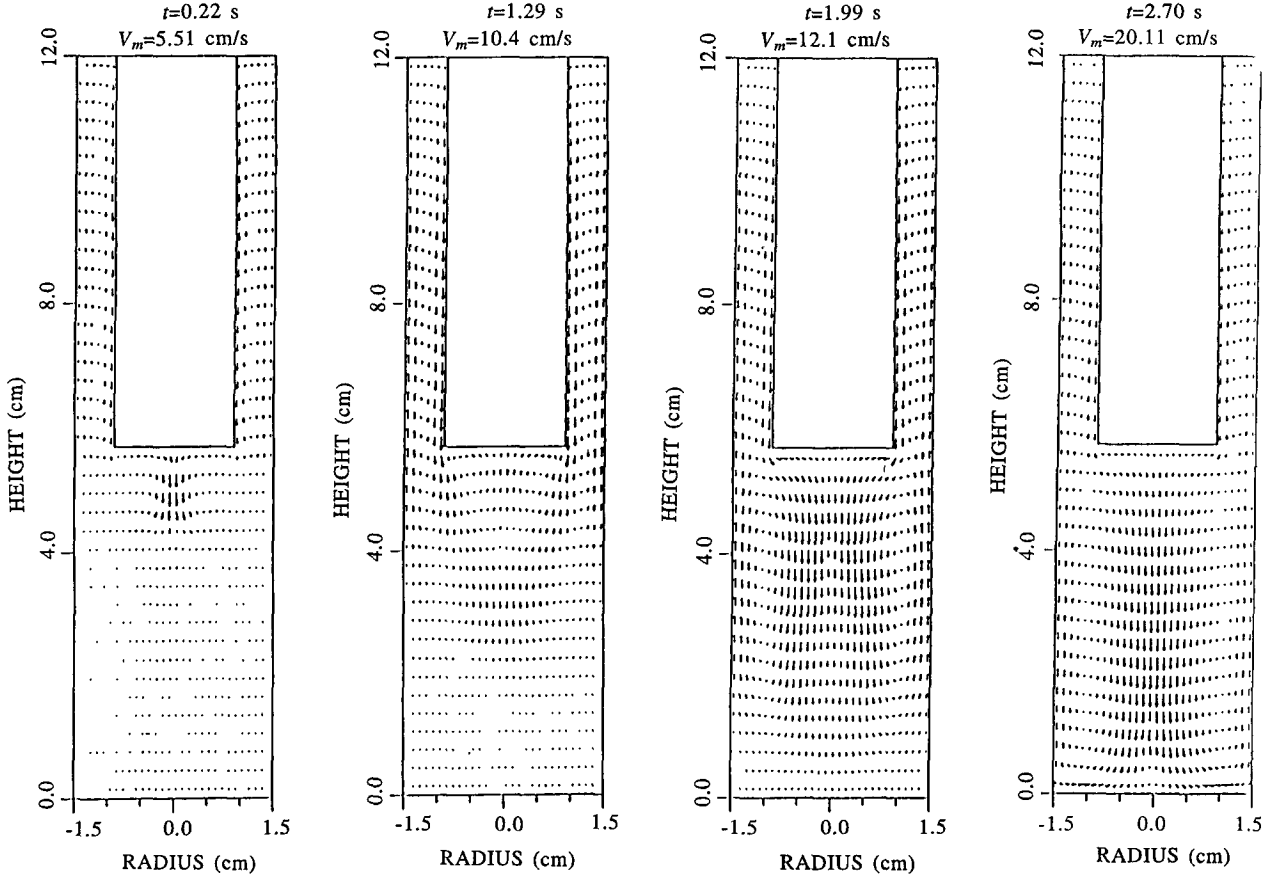
Fig. 2. Flow profile initiation and development in the $r$-$z$ plane at $\theta=0°$ and $180°$ under normal direction ($\psi=0°$) gravitational acceleration.

have been developed and illustrated in our earlier studies (Hung et al., 1992a, 1992b, 1992c, 1992d, 1993a, 1993b, 1994a, 1994b, 1994c, 1994d, 1994e) and will not be repeated. The time step is determined automatically based on the size of the grid points and the velocity of the flow fields. As the thickness of the boundary layer is inversely proportional to the square root of the Reynolds number, the size of the grid points shall be adjusted according to the flow fields of the Reynolds number. In other words, the size of the grid points shall be smaller as the flow fields of the Reynolds number become greater. Failure to adjust the size of the grid points on the basis of increasing Reynolds numbers will result in numerical instabilities which will have great impact on local oscillations (Kitchens et al., 1978; Kitchens, 1980; Hung and Pan, 1995). Special care shall be used to eliminate these numerical instabilities by properly adjusting the size of the grid points, which will eventually contribute to the adjustment of time steps. It is needless to say that the development of

real physical instability will certainly occur at a higher Reynolds number since contributions by viscosity effects to damping of flow disturbances will be reduced. It is very important for us to distinguish the differences between numerical and real physical instabilities, particularly for flows with high Reynolds numbers.

In this study, two sets of grids, with grids of $17\times34\times42$ and $23\times34\times82$ along the ($r$, $\theta$, $z$) coordinates, have been designed to carry out numerical computations. For a Reynolds number of 150 with a maximum induced velocity of 0.2 m/s, as in the present case, there is no difference for numerical results obtained for either grid chosen. By using the grids of $17\times34\times42$ in the computation of flows with higher Reynolds numbers such as $Re\geq1500$ with an induced velocity of 2.0 m/s and higher extremely severe numerical instabilities of the flow field result. With grids of $17\times34\times42$, the average time step determined from the size of the grid points and the velocity of the flow fields is 0.0007 s while the
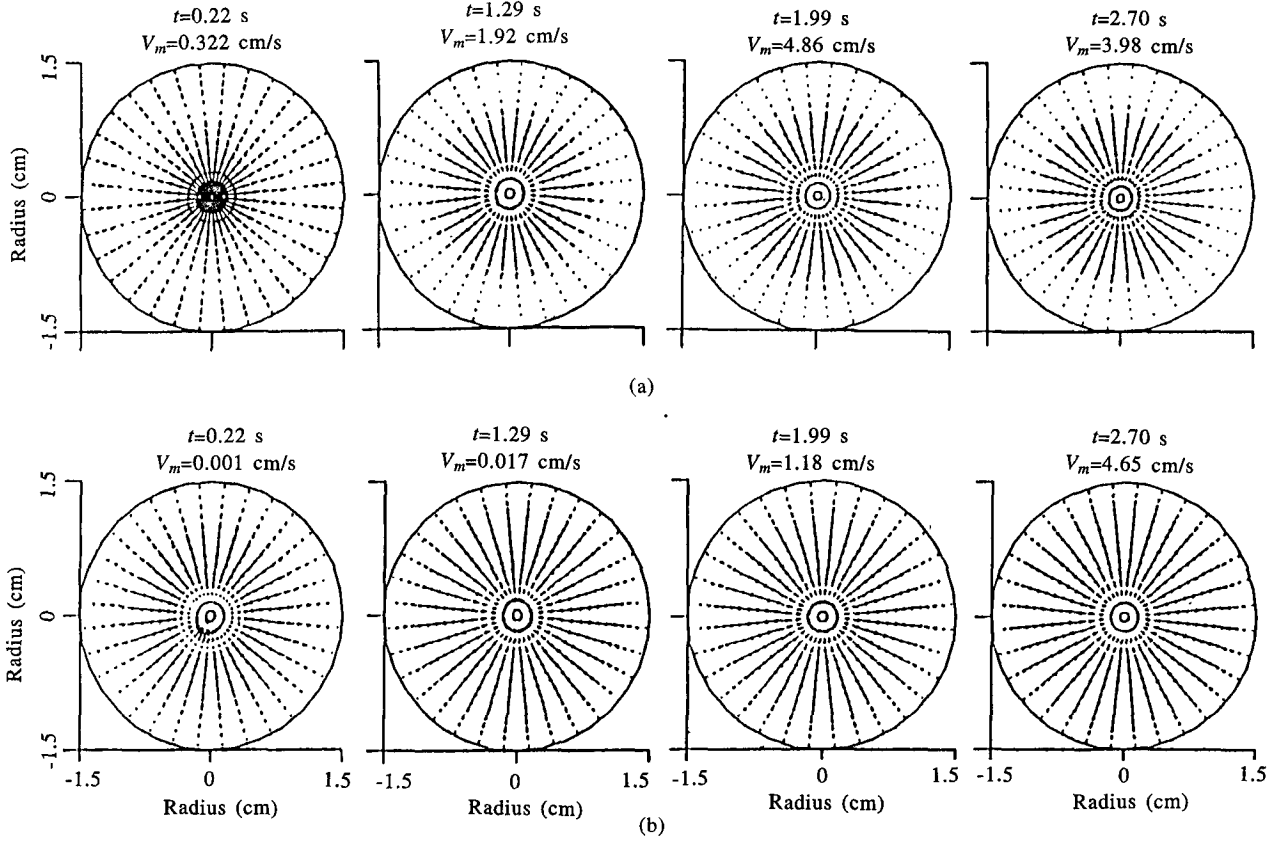
Fig. 3. Flow profile initiation and development (a) in the $r-\theta$ plane at $z$=5.55 cm under normal direction ($\psi$=0°) gravitaitonal acceleration; and (b) in the $r-\theta$ plane at $z$=0.45 cm under normal direction ($\psi$=0°) gravitational acceleration.

CPU time required by a CRAY II supercomputer to execute one time step is 3.019 s. The total CPU time consumed for each of the three cases in this study is 12000 s.

In this study, the directions of the background gravity along the three different directions with $\psi$=0°, 45° and 180° along the $r-z$ plane with $\theta$=0° are chosen as orientations to investigate the characteristics of convection-driven flow and temperature profiles.

Various references have been cited by Bejan (1995) in the study of induced convective heat transfer with fluid layers heated from below, top, side, oblique etc. under normal atmospheric pressure. As mentioned in the Introduction, this study investigated the time dependence from initiation and formation of flow fields and the temperature distribution throughout the vapor deposition process. The objective was to determine the sensitivity of the formation of nonlinear optical thin films to convection in a relatively low pressure environment of $10^{-2}$ mmHg (Paley et al., 1992). To our knowledge, there

have been no studies on induced convective heat transfer at relatively low pressure; hence, there is no available literature for comparison. However, there is quali-tative agreement of flow profiles and temperature distributions for induced convection at both normal atmospheric pressure and $10^{-2}$ mm Hg low pressure.

## 1. Convection Driven by the Normal Direction ($\psi$=0°) to Gravitational Acceleration

The time animation of the development of flow fields under bottom heating, i.e., the normal direction ($\psi$=0°) of gravitational acceleration, is illustrated in Fig. 2 for convection-induced flow vectors (in terms of the directions and magnitudes of convection induced-flow velocities) in the $r-z$ plane. The maximum velocity represented by each subfigure is specified separately in the corresponding subfigure. For convenience of comparison, in the Fig. 2, 4 subfigures condense all the flow patterns at time sequences $t$=0.58, 1.72, 2.39, and 3.10 s. The following results
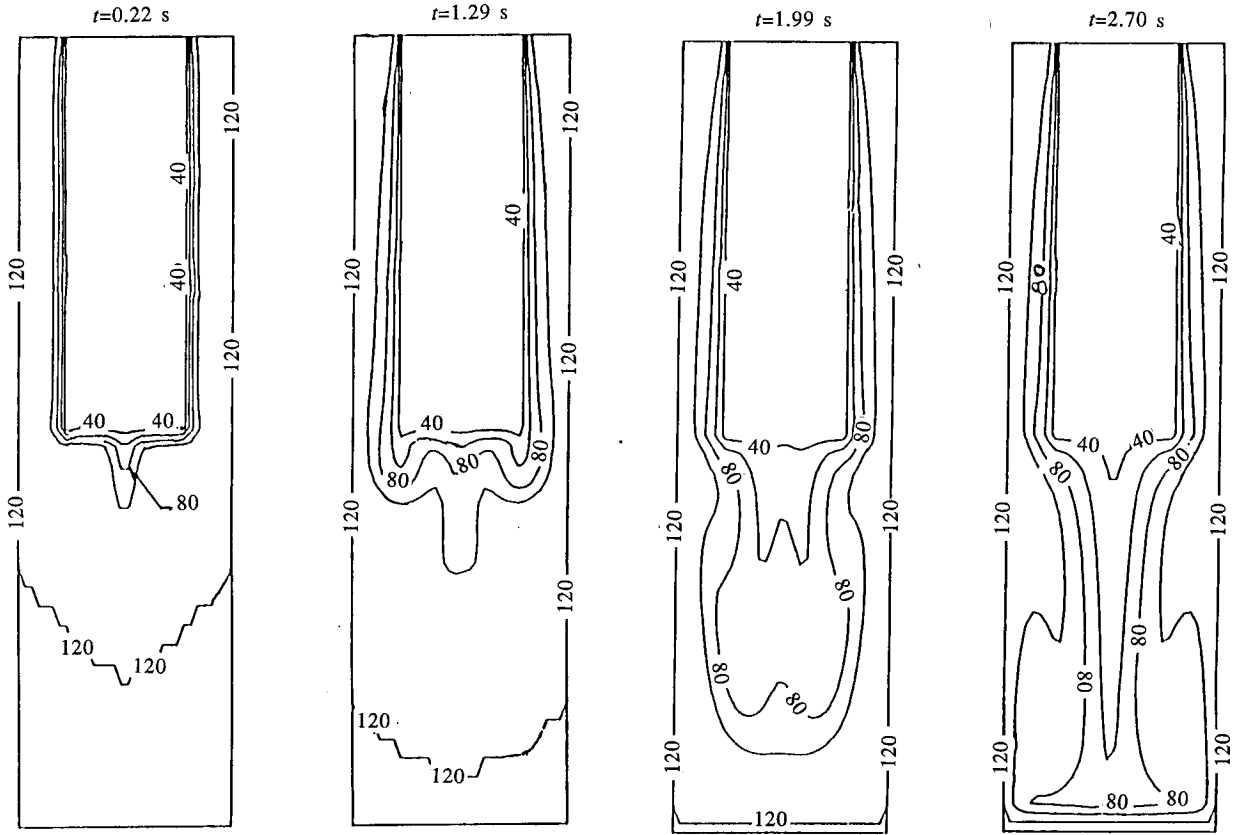
**Fig. 4.** Initiation and formation of a temperature profile in the $r$–$z$ plane at $\theta=0°$ and $180°$ under normal direction ($\psi=0°$) gravitational acceleration.

summarize the flow patterns in this series of subfigures in Fig. 2: (1) A convection induced downward flow toward the bottom of the outer cylinder with an inflow stream is initiated at the bottom of the central column at time $t<0.2$ s (not shown). (2) A convection induced downward flow along the surface of the inner cylinder with inflow from the surface of the outer cylinder toward the surface of the inner cylinder (at the upper section of the container within the slender gap between the co-axial cylinders) is also initiated during the time period of 0.2 s$<t<0.4$ s. (3) A convection induced flow pattern of upward flow along the surface of the outer cylinder and downward flow along the surface of the inner cylinder (central column) is gradually formed (at the upper section of the container within the slender gap between the co-axial cylinders) with intensified flow velocities. This downward flow is accompanied by a stream of inflow from the surface of the outer cylinder to the inner cylinder during the time period of 0.2 s$<t<0.9$ s. (4) A convection-induced inflow pattern toward the center of the axial coordinate at the

upper section of the container with a height of $z>2.7$ cm, and an outflow pattern toward the surface of the outer cylinder at the lower section of the container with a height of $z<2.7$ cm are gradually formed for time $t>0.9$ s. (5) A convection induced flow pattern of two recirculation flows has centers at $(r_c, z_c)=(\pm1.9, 2.7)$ cm, where $r_c$ and $z_c$ denote the centers of recirculation flow along the $r$- and $z$-coordinates, respectively. The circulation direction of the left-hand-side induced convection recirculation flow is clockwise while that of the right-hand-side induced convection recirculation flow is counter-clockwise for time $t>1.3$ s.

Figure 3(a) and (b) illustrate the flow patterns of convection induced inflow and outflow. Figure 3(a) shows the time animation of initiation and development of convection induced inflow in the region below the central column (at $z=5.55$ cm). Figure 3(b) shows convection induced outflow in the region near the bottom of the outer cylinder (at $z=0.45$ cm). Figure 3(a) and (b) also show convection induced flow vectors (in terms of the directions and mag-

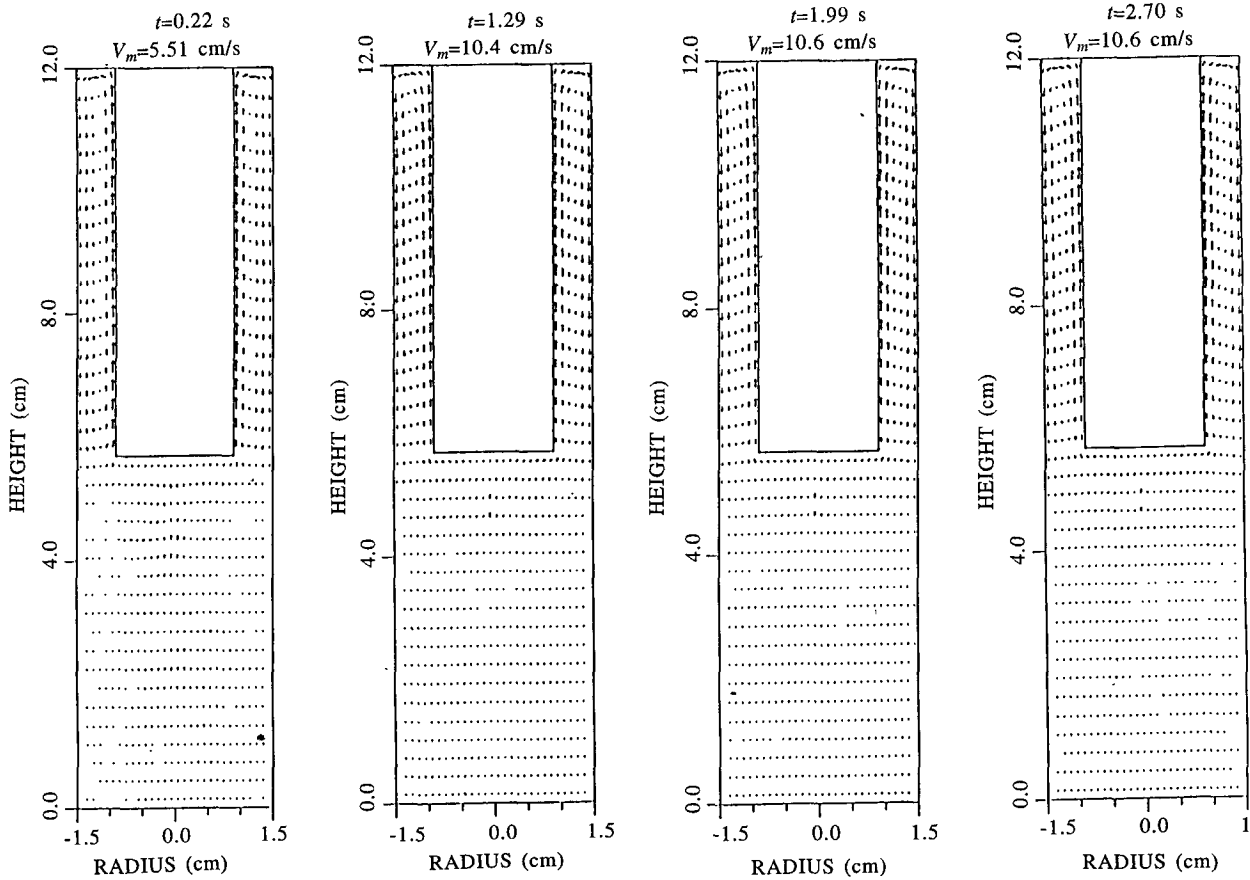**Fig. 5.** Flow profile initiation and development in the $r$–$z$ plane at $\theta$=0° and 180° under reverse normal direction ($\psi$=180°) gravitational acceleration.

nitudes of induced flow velocities) in the $r$–$\theta$ ($x$–$y$) plane. The maximum velocity for each subfigure is also specified separately in the corresponding subfigure. It is interesting to note that there is an induced inflow zone with flow from the surface of the outer cylinder inward toward the center located at the upper section of the container for heights at $z$>2.7 cm. There is also an induced outflow zone with flow from the center toward the surface of the outer cylinder at the lower section of the container for heights at $z$<2.7 cm. Before the induced flow is developed to such a clear-cut flow zone of (1) an upper part with inflow and (2) a lower part with outflow for the flow approaching steady-state from transient formation, there is an induced temporary flow pattern at the beginning of flow formation. Figure 3(a) shows that there is induced temporary outflow is formed at the exterior region of the container near the surface of the outer cylinder at the very beginning of flow initiation. This induced flow zone disappears quickly as flow development nears steadystate. Obviously, the major vapor deposition at the bottom surface of the central

column is contributed by the induced inflow from exterior flow zones which are brought upward along the bottom surface of the outer cylinder. In other words, the flow analysis indicates that vapor deposition at the bottom surface of the central column does not result from direct upward diffusion from the source materials stored at the bottom surface of the outer cylinder. It is, rather, a vapor deposition process resulting from a fairly complicated induced flow pattern of recirculation.

Figure 4 shows a time animation of the initiation and formation of temperature profiles due to induced convection in the $r$–$z$ plane at $\theta$=0° and 180° during the course of the entire induced flow region development. The curves shown in Fig. 4 are the isothermal lines with values of temperature indicated in °C at the corresponding locations. The results of comparison of Figs. 2 to 4 can be summarized as follows: (1) At time $t$=0 (not shown), there is very sharp temperature distribution variance from 30 to 120°C in a fairly thin layer. (2) An initiation of downward flow from the bottom of the central column toward the bottom of the outer cylinder immediately creates a gradually expand-
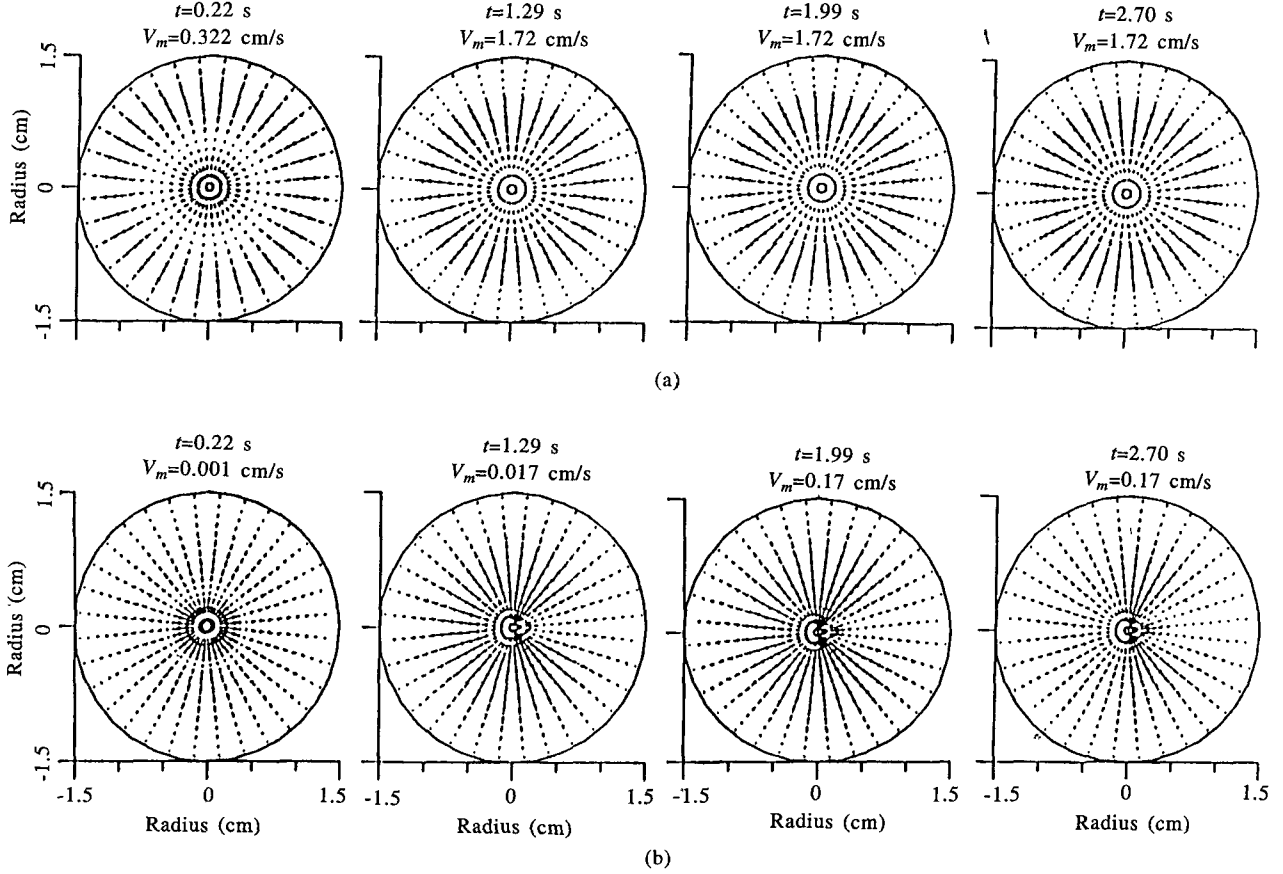
**Fig. 6.** Flow profile initiation and development (a) in the $r-\theta$ plane at $z=5.55$ cm under reverse normal direction ($\psi=180°$) gravitational acceleration; and (b) in the $r-\theta$ plane at $z=0.45$ cm under reverse normal direction ($\psi=180°$) gravitational acceleration.

ing positive temperature gradient along the downward directions for time $t>0.1$ s. (3) A flow pattern of induced inflow from the surface of the outer cylinder toward the center of the axial coordinate promotes a parabolic shape temperature profile with the tip located around the center of the axial coordinate downward toward the bottom of the outer cylinder due to the induced downward cold streams from the bottom of the centeral column toward the bottom of the outer cylinder for the time $t>0.1$ s. (4) An induced upward profile of temperature distribution at the exterior region around the surface of the outer cylinder is a result of an upward flow pattern along the corresponding outer surface of the cylinder. (5) An induced downward profile of temperature distribution immediately around the neighborhood of the surface of the inner cylinder (central column) is a result of the induced downward flow pattern along the corresponding surface of the central column.

## 2. Convection Driven by the Reverse Normal Direction ($\psi=180°$) to Gravitational Acceleration

The time animation of the development of induced flow fields upon top heating, i.e., the reverse normal direction ($\psi=180°$) to gravitational acceleration, is illustrated in Fig. 5 for convection induced flow vectors (in terms of the directions and magnitudes of induced flow velocities) in the $r-z$ plane. The maximum velocity represented by each subfigure is specified separately in the corresponding subfigure. This problem can be divided into two sections with upper and lower regions for flow fields induced by the reverse normal direction ($\psi=180°$) gravitational acceleration. In the upper region for $z>6$ cm, the problem can be associated with horizontal heating from the walls of the outer cylinder toward the walls of the inner cylinder in a flow zone within the narrow cylindrical slit of space. In the lower region for $z<6$ cm, the problem is that of vertical heating from the top (downward gravity direction). As the source materical is located at the surface of $z=0$, and the location of vapor deposition is at the bottom horizontal surface of the central column at $z=6$ cm, the upper flow profile in $z>6$ cm has very little effect on the flow
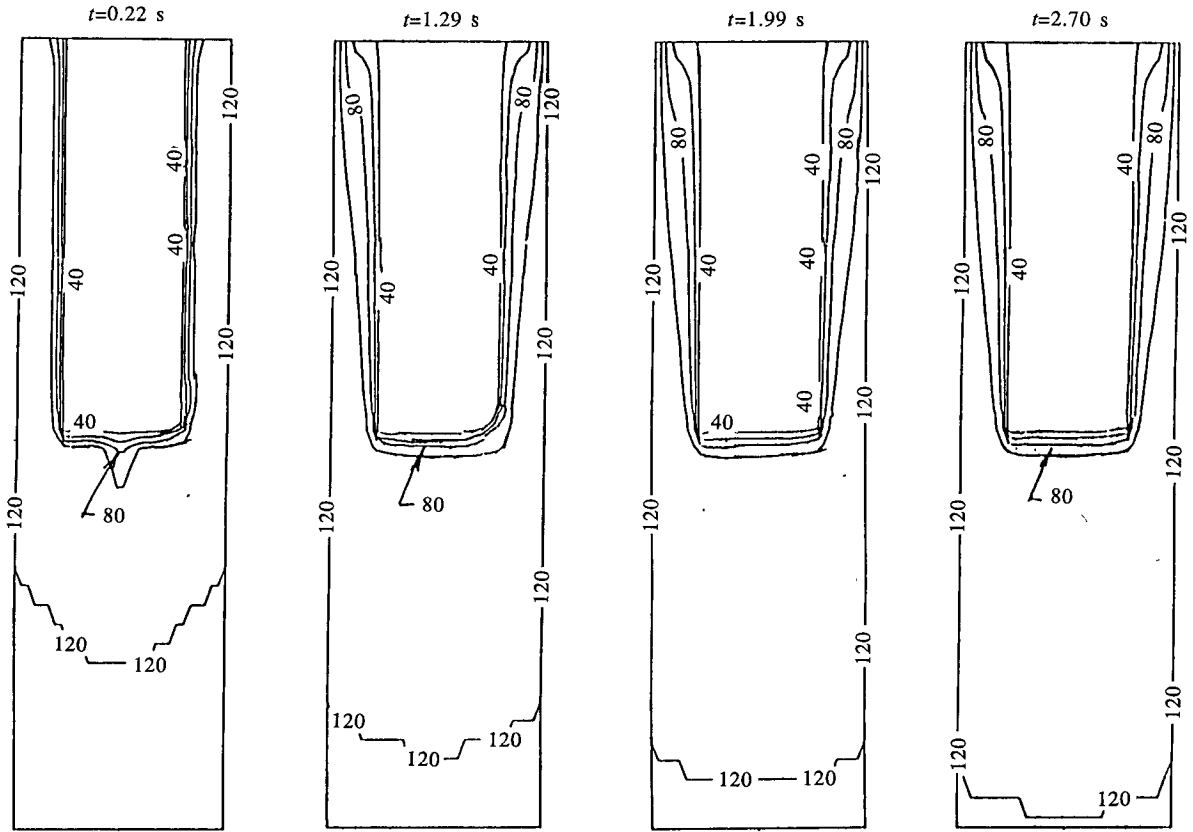
**Fig. 7.** Initiation and formation of a temperature profile in the $r-z$ plane at $\theta=0°$ and 180° under reverse normal direction ($\psi=180°$) gravitational acceleration.

pattern formation of vapor deposition. Thus, we can ignore the flow profiles induced within a narrow cylindrical slit of space. As to the lower flow region at $z<6$ cm, Fig. 5 shows that stably stratified medium and natural convection is completely prohibited.

For the reverse normal direction to gravitational acceleration, Fig. 6(a) and (b) show the time animation of initiation and development of outflow in the region below the central column (at $z=5.55$ cm) and inflow in the region near the bottom of the outer cylinder (at $z=0.45$ cm), respectively. Figure 6(a) and (b) also show flow vectors (in terms of the directions and magnitudes of induced flow velocities) in the $r-\theta$ ($x-y$) plane. The maximum velocity for each subfigure is specified separately in the corresponding subfigure. Comparison of Figs. 5 and 6 shows some interesting results as follows: (1) Practically, there is no induced flow field for natural convection along the vertical direction, and only a stratified medium is shown in the $r-z$ plane for $z<6$ cm due to the phenomena of vertical heating from the top (downward gravity direc-

tion). (2) There is a very small induced flow along the horizontal direction in the $r-\theta$ plane for $z>6$ cm due to heating from the side walls. There is a slightly larger flow at the top than at the bottom in this region due to the low temperature of the central column at $z>6$ cm.

Figure 7 shows the time evolution of initiation and formation of temperature profiles driven by the reverse normal direction ($\psi=180°$) to gravitational acceleration in the $r-z$ plane at $\theta=0°$ and 180°. The curves in Fig. 7 are the isothermal lines with temperature indicated in °C at the corresponding locations. Again, the figure clearly shows two regions between the upper and lower parts. For the upper region $z>6$ cm, horizontal heating from the side walls drives the convective flow toward the central wall within a narrow cylindrical slit. Figure 9 depicts a series of isothermal curves with decreasing temperature from the side walls toward the central column. As indicated earlier, this region is not important in our study of vapor deposition from source materials located on the surface at $z=0$ transferring vapor and forming thin films at the bottom of the central
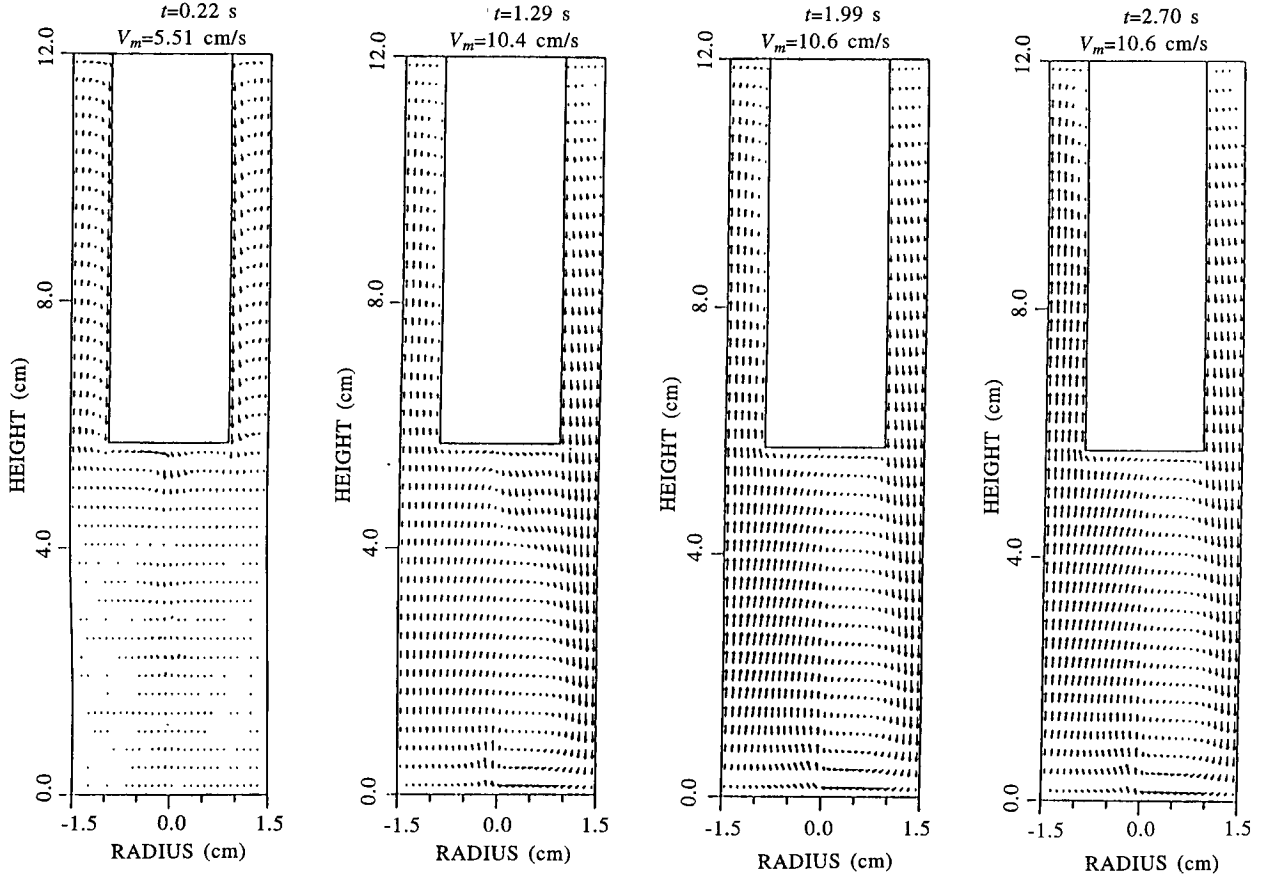
**Fig. 8.** Flow profile initiation and development in the $r-z$ plane at $\theta=0°$ and $180°$ under oblique direction ($\psi=45°$) gravitational acceleration.

column at $z=6$ cm. On the other hand, there is not much variation in the dynamics of the temperature distribution for the lower region $z<6$ cm because the region is filled with the stably stratified medium, and natural convection is completely prohibited.

## 3. Convection Driven by the Oblique Direction at 45° to Gravitational Acceleration

In this case, the cell is allowed to tilt at 45° relative to gravitational acceleration, the $r-z$ plane, with $\theta=0°$. In other words, the induced flow profile shown in Fig. 8 places the $r-z$ plane at $\theta=0°$ and $180°$. The illustration is that of convective flow induced by a vector summation of gravitational acceleration with a horizontal component at 0.707 $g_o$ ($g_o\sin45°$) rightward and a vertical component at 0.707 $g_o$ ($g_o\cos45°$) downward. On the other hand, the induced flow profile shown in Fig. 9 with the $r-z$ plane at $\theta=90°$ and 270° shows convective flow induced by reduced gravity acceleration component with a magnitude of 0.707 $g_o$ downward.

Comparison of Figs. 2 and 8 shows the following results: (1) There is a downward flow toward the bottom of the outer cylinder with an inflow stream initiated at the bottom of the central column for both normal and oblique gravitational accelerations at time $t<0.2$ s. (2) A downward flow along the surface of the inner cylinder with inflow from the surface of the outer cylinder toward the surface of the inner cylinder (at the upper section of the container within the slender gap between the co-axial cylinders) occurs for both normal and oblique gravitational accelerations during the time period $0.2$ s$<t<0.4$ s. (3) Patterns of upward flow along the surface of the left-side outer cylinder and downward flow along both surfaces of the inner cylinder (central column) and the right-side outer cylinder are gradually formed (at the upper section of the container within the slender gap between the co-axial cylinders). Flow velocities are intense and are accompanied by a stream of inflow at the left side from the surfaces of the outer cylinder to the inner cylinder, and by outflow at the right-side from the surfaces of the inner cylinder to the outer
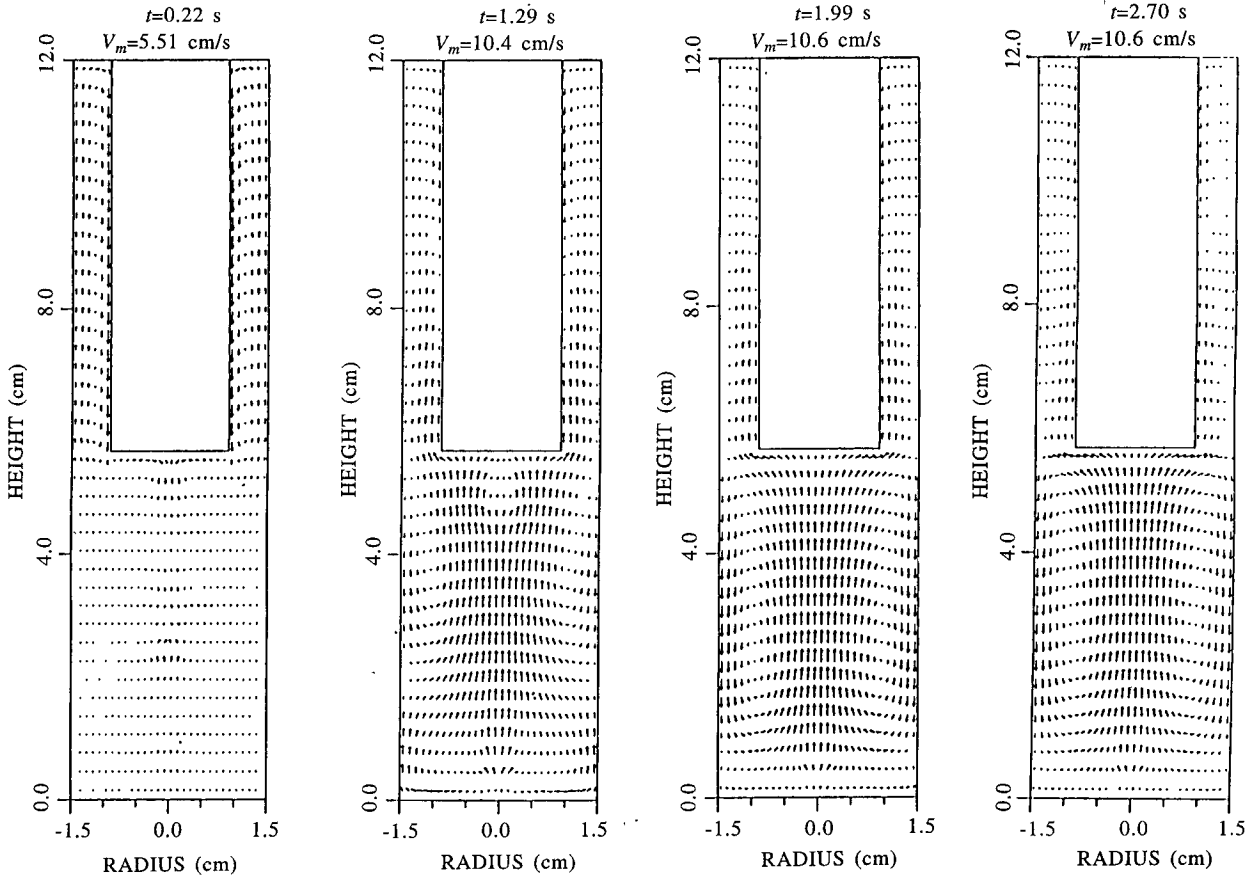
**Fig. 9.** Flow profile initiation and development in the $r$–$z$ plane at $\theta$=90° and 270° under oblique direction ($\psi$=45°) gravitational acceleration.

cylinder. These flows are driven by a 45° direction oblique to the gravitational acceleration during the time period of 0.2 s<$t$<0.9 s. This asymmetric flow profile is quite different from the symmetric flow profile resulting from the $\psi$=0° direction, the normal gravity acceleration. (4) An inflow pattern at the left-side and outflow at the right-side for a height of $z$>1.2 cm, and an outflow pattern at the left-side, and inflow at the right-side for a height of $z$<1.2 cm are gradually formed for time $t$>0.9 s. (5) There is a pattern of asymmetric recirculation flow with its center at ($r_c$, $z_c$)=(0.6, 1.2) cm, where $r_c$ and $z_c$ denote the center of the recirculation flow along the $r$- and $z$-coordinates, respectively. The direction of the recirculation flow is clock-wise during time $t$>1.2 s.

In contrast to Fig. 8 for an induced asymmetric flow profile in the $r$–$z$ plane at $\theta$=0°–180° and $\psi$=45° to an oblique direction gravitational acceleration, Fig. 9 shows an induced symmetric flow profile in the $r$–$z$ plane at $\theta$=90°–270° due to a reduced 0.707 $g_o$ gravity acceleration in the downward direction. Comparison of Figs. 2 and 9 shows differ-

ences in induced flow fields driven by normal (1 $g_o$) and reduced (0.707 $g_o$) gravitational accelerations. The major differences are as follows: (1) Upward motions along the surface of the outer cylinder are shown for flow induced by the normal gravity acceleration while similar upward motions around the central axis of the cylinder result from flow induced by the reduced gravity acceleration. (2) Downward motions around the central axis of the cylinder are illustrated for flow induced by normal gravity accelerations while the upward motion around the central axis of the cylinder accompanied by downward motion along the surfaces of both sides of the outer cylinder result from flow induced by the reduced gravity. (3) There are two recirculation flows generated with centers at ($r_c$, $z_c$)= (±1.9, 2.7) cm and at ($r_c$, $z_c$)=(±0.8, 3.2) cm for flows induced by normal and reduced gravity accelerations, respectively. (4) The flow directions of the left-hand side and right-hand side recirculation zones are clockwise and counter-clockwise, respectively, for flows induced by the reduced gravity acceleration. These different results in the patterns
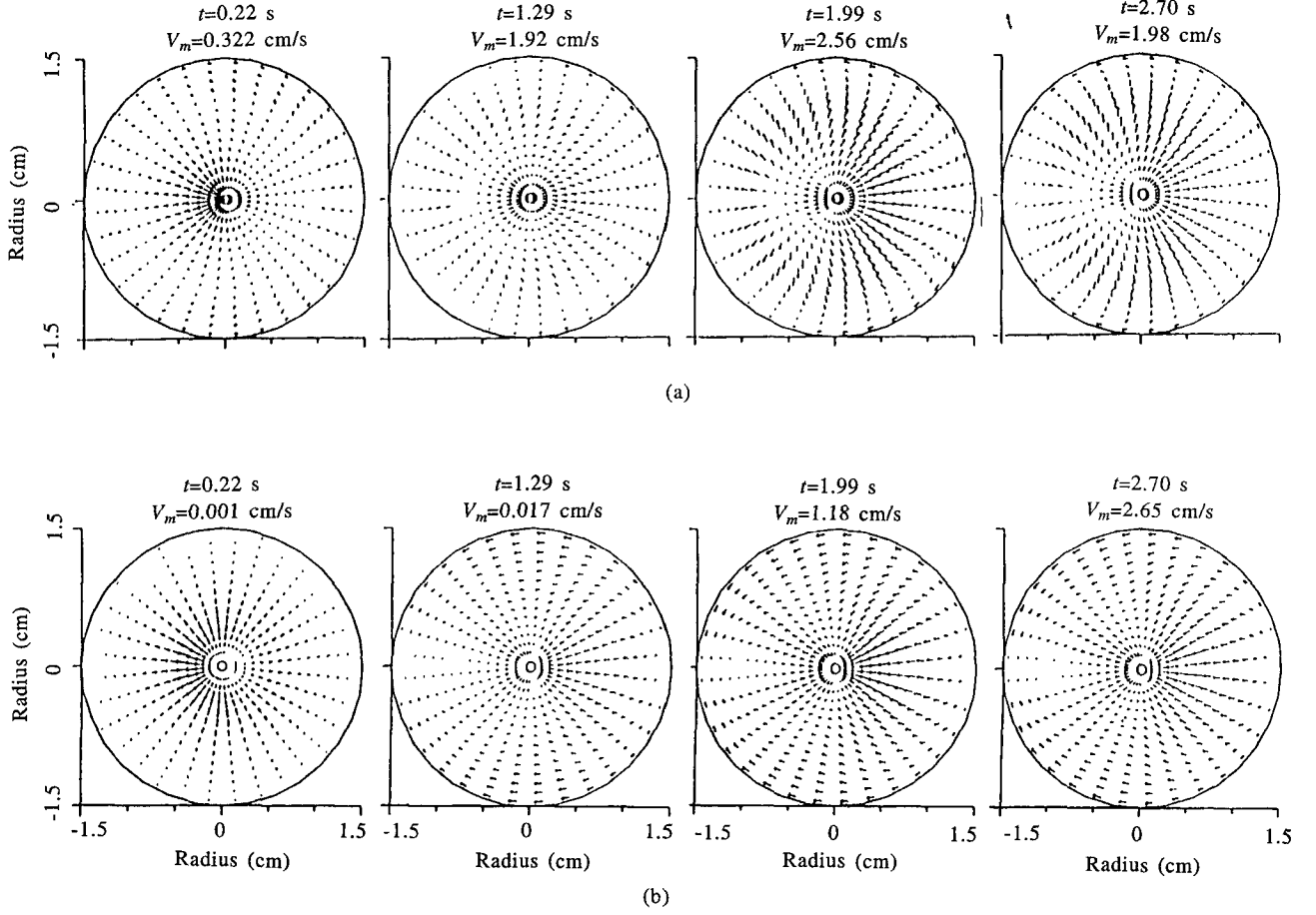
−31−

**Fig. 10.** Flow profile initiation and development (a) in the $r-\theta$ plane at $z$=5.55 cm under oblique direction ($\psi$=45°) gravitational acceleration; and (b) in the $r-\theta$ plane at $z$=0.45 cm under oblique direction ($\psi$=45°) gravitational acceleration.

of flow recirculation show a very important finding that the reduced gravity can help in promoting direct transport of source materials at the bottom of the outer cylinder to the location of vapor deposition at the ·bottom of the central column without going through the complicated flow profiles of a transport process performed under normal gravity environment.

To illustrate the flow patterns of inflow and outflow, Fig. 10(a) and (b) show the time animation of initiation and development mostly of outflow in the region immediately below the central column (at $z$=5.55 cm) and mostly of inflow in the region near the bottom of the outer cylinder (at $z$=0.45 cm), respectively. Figure 10(a) and (b) also show flow vectors (in terms of the directions and magnitudes of induced flow velocities) in the $r-\theta$ ($x-y$) plane. The maximum velocity for each subfigure is specified separately in the corresponding subfigure. It is interesting to note that there is a flow zone with mostly outflow from the region around the central axis of

the cylinder outward toward the direction of the surface of the outer cylinder with a location at the upper section of the container for heights of $z$>0.8 cm. There is also a zone with mostly inflow from the surface of the outer cylinder toward the central axis at the lower section of the container for heights of $z$<0.8 cm. The horizontal component of gravitational acceleration of 0.707 $g_o$ contributes to the initiation of very complicated flow profiles, shown in Fig. 10(a) and (b), where there are inflow components shown for heights of $z$>0.8 cm, and outflow components shown for heights of $z$<0.8 cm in the range $135°<\theta$ $<225°$. In other words, because of the horizontal components to gravitational acceleration due to an oblique orientation with respect to gravity acceleration, vapor deposition at the bottom surface of the central column is a combination of (1) inflow from external flow zones of the cylinder in the range $135°<\theta<225°$ which are brought upward along the surface of the outer cylinder due to sublimation of source materials stored at the bottom surface of the outer cylinder,
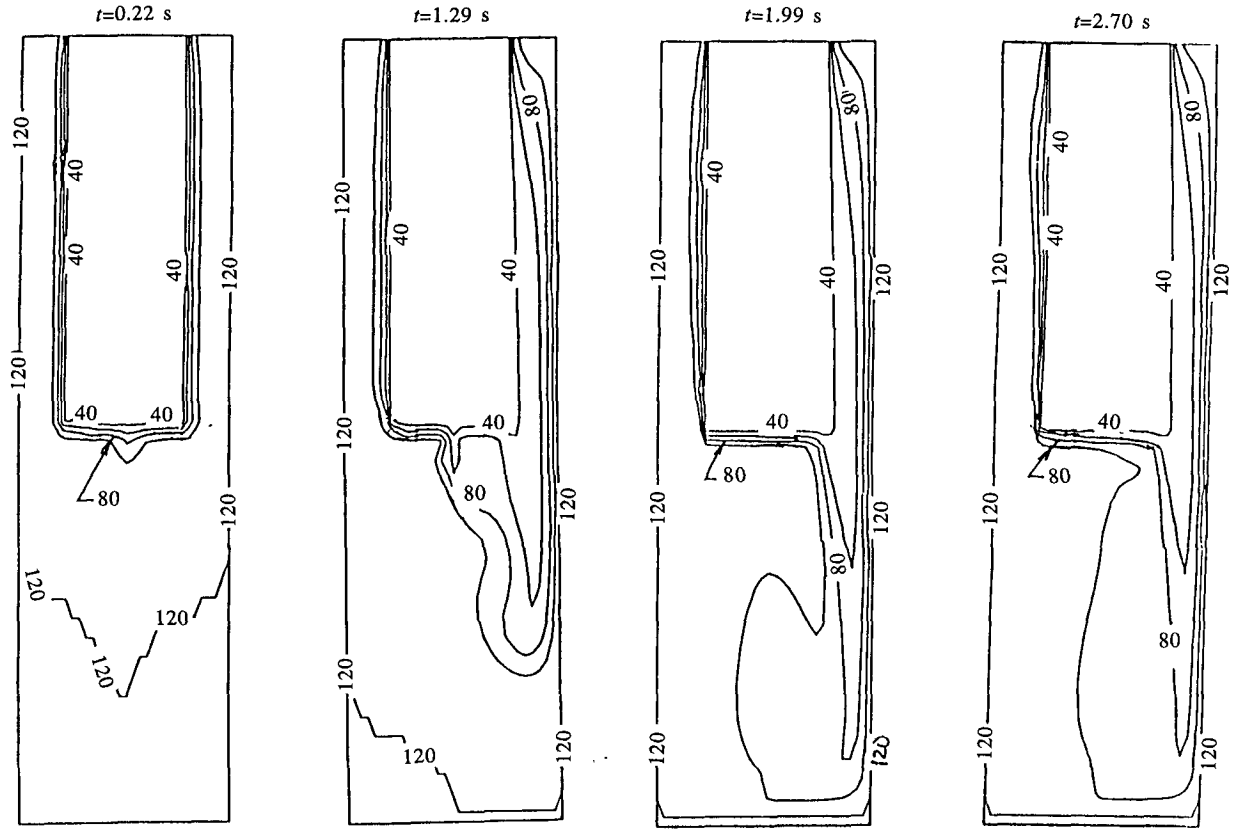
**Fig. 11.** Initiation and formation of a temperature profile in the $r$–$z$ plane at $\theta=0°$ and $180°$ under oblique direction ($\psi=45°$) gravitational acceleration.

and (2) the direct transport of source materials with upward flow from the bottom surface of the outer cylinder to the location of vapor deposition in the ranges of $\theta<135°$ and $\theta>225°$. In other words, the flow analysis indicates that vapor deposition at the bottom surface of the central column benefits from direct straight upward diffusion from the evaporation of source materials stored at the bottom surface of the outer cylinder exposed to the oblique direction gravitational acceleration in the ranges of $\theta>225°$ and $\theta<135°$. In other words, obliqued direction gravitational acceleration can not completely secure better quality vapor deposition because of the presence of the horizontal component of gravitational acceleration.

Figures 11 and 12 show the time animation of initiation and formation of temperature profiles in the $r$–$z$ plane at $\theta=0°$–$180°$ and at $\theta=90°$–$270°$, respectively, during the course of the entire flow region development under oblique direction gravitational acceleration. Figure 11 shows the temporal variation of isothermal lines resulting

from the combination of rightward and downward gravity accelerations. It shows clearly the initiation and development of isothermal lines with a combination of rightward and downward movements. Comparison of Fig. 8 for the velocity profile and Fig. 11 for the temperature profile illustrates very interesting similarity between these two groups of curves.

Figure 12 shows the similar temporal variation of isothermal lines from another angle point of view which results from reduced gravity acceleration with a magnitude of 0.707 $g_o$. Initiation and development of the cone shape temperature profile results from a direct upward induced flow from the bottom surface of the outer cylinder toward the bottom surface of the central column. The temperature profiles shown in Fig. 12 and the flow profile shown in Fig. 9 strongly suggest that the vapor deposition under a reduced gravity environment may be able to promote material processing of vapor deposition with a homogeneous crystalline film with fine
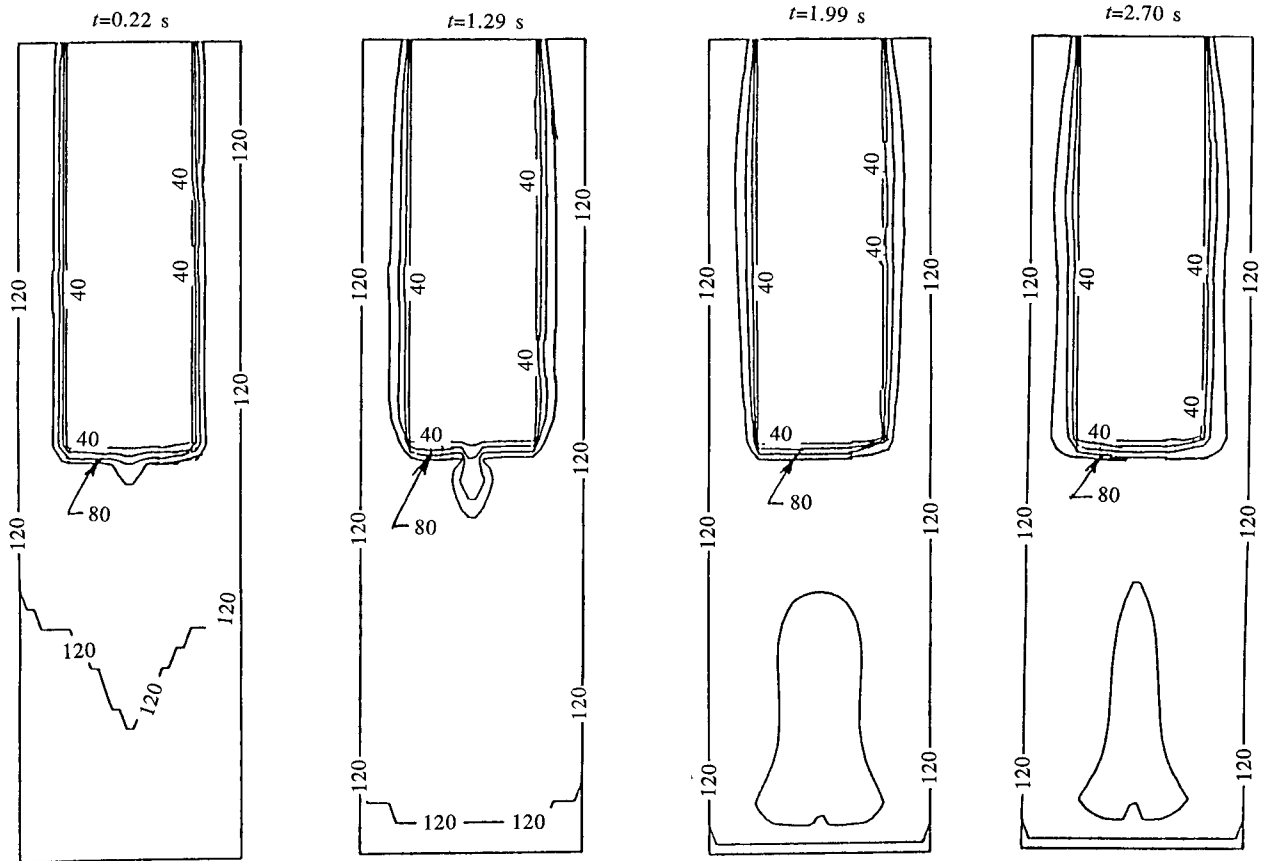
**Fig. 12.** Initiation and formation of a temperature profile in the $r$–$z$ plane at $\theta=90°$ and $270°$ under oblique direction ($\psi=45°$) gravitational acceleration.

grains.

## IV. Discussion and Conclusion

In this study, mathematical formulations of the initiation and development of fluid profiles and temperature distributions driven by the heat transfer process of natural convection under normal and oblique directions of gravitational acceleration with an extremely low pressure environment have been examined. The purpose of present study was to investigate the characteristics of vapor deposition under a low pressure environment to be used to promote the processing of nonlinear optical materials by growing homogeneous fine grains of thin crystalline films of diacetylene monomer (Nayar and Winter, 1990). Numerical computation of a full set of non-linear fluid dynamics shows that the vapor deposition process has to be accomplished through a fairly complicated flow pattern of recirculation under a normal gravity environment both in normal and oblique directions which are the major driving

forces to induce natural convection in a low pressure environment. For the case of natural convection under normal gravitational acceleration with an oblique direction along a plane perpendicular to the gravity acceleration, the results show the possibility of inducing a simple direct updraft motion to transport source materials from the location of storage to the location of vapor deposition under a reduced gravitational acceleration in the ranges of $\theta<135°$ and $\theta>225°$. The oblique direction gravitational acceleration is always accompanied by a component of gravitational acceleration in the horizontal direction, which excites complicated flow patterns in the regions of $135°<\theta<225°$. The existence of a horizontal component of gravitational acceleration is unavoidable for any experiment subjected to oblique direction gravity. It can be anticipated that there is no way to produce completely homogeneous thin crystalline films with fine grains under such a complicated flow pattern of recirculation with a nonuniform temperature distribution in a normal gravity environment. This study suggests

-34-

that it is necessary to adopt a unique environment with microgravity to eliminate natural convection. In so doing, we can carry out an experiment which can simplify the flow pattern and reach a goal of producing homogeneous thin films with fine grains in future space experiments. Numerical study of fluid mechanics computation can be used to determine the best experimental method with the best setup to achieve the goal of processing the best quality nonlinear optical materials in future space experiments.

## Acknowledgment

## References

Bejan, A. (1995) *Convection Heat Transfer*, 2nd Ed., p. 623. Wiley, New York, NY, U.S.A.

Carter, G.M., Y. J. Chen, and S. K. Tripathy (1983) Intensity-dependent index of refraction in multilayers of polydiacetylene. *Appli. Phys. Lett.*, **43**, 891-893.

Hung, R. J., K. L. Shyu, and C. C. Lee (1992a) Medium-frequency impulsive-thrust-activated liquid hydrogen reorientation with geyser. *Journal of Propulsion and Power*, **8**, 778-785.

Hung, R. J., K. L. Shyu, and C. C. Lee (1992b) Liquid hydrogen slosh wave excited by constant reverse gravity acceleration of geyser initiation. *Journal of Spacecraft and Rockets*, **29**, 523-528.

Hung, R. J., C. C. Lee, and F. W. Leslie (1992c) Spacecraft dynamical distribution of fluid stresses activated by gravity—jitter-induced slosh waves. *Journal of Guidance, Control and Dynamics*, **15**, 817-824.

Hung, R. J., C. C. Lee, and F. W. Leslie (1992d) Similarity rules in gravity jitter-related spacecraft liquid propellant slosh waves excitation. *Journal of Fluids and Structures*, **6**, 493-522.

Hung, R. J., C. C. Lee, and F. W. Leslie (1993a) Effect of the baffle on the spacecraft fluid propellant viscous stress and moment fluctuations. *Transaction of the Japan Society for Aeronautical and Space Sciences*, **35**, 187-207.

Hung, R. J., C. C. Lee, and F. W. Leslie (1993b) Effect of the baffle on the asymmetric gravity-jitter excited slosh waves and spacecraft moment and angular momentum fluctuations. *Journal of Aerospace Engineering*, **207**, 105-120.

Hung, R. J. and H. L. Pan (1995) Three-dimensional transient flow

of spin-up in oblique gravity force. *Transaction of the Japan Society for Aeronautical and Space Sciences*, **38**, 136-150.

Hung, R. J., H. L. Pan, and F. W. Leslie (1994a) Gravity gradient or gravity jitter induced viscous stress and moment fluctuations in microgravity. *Fluid Dynamics Research*, **14**, 29-51.

Hung, R. J., H. L. Pan, and F. W. Leslie (1994b) Fluid system angular momentum and moment fluctuations driven by gravity gradient or gravity jitter in microgravity. *Journal of Flight Sciences and Space Research*, **18**, 195-202.

Hung, R. J., H. L. Pan, and Y. T. Long (1994c) Slosh dynamics modulated cryogenic helium fluids driven by gravity gradient or jitter accelerations associated with slew motion in microgravity. *Acta Mechanica Sinica*, **10**, 367-381.

Hung, R. J., H. L. Pan, and Y. T. Long (1994d) Peculiar behavior of helium II disturbances due to sloshing dynamics driven by jitter accelerations. *Cryogenics*, **34**, 641-648.

Hung, R. J., Y. T. Long, and H. L. Pan (1994e) Sloshing dynamics induced angular momentum fluctuations driven by jitter accelerations associated with slew motion in microgravity. *Transactions of Japan Society for Aeronautics and Space Sciences*, **37**, 217-234.

Kajzar, F., J. Meissier, J. Zyss, and I. Ledoux (1983) Nonlinear interferometry in Langmuir-Blodgette multilayers of polydiacetylene. *Opt. Commun.*, **45**, 133-137.

Kajzar, F. and J. Meissier (1988) Resonance enhancement in cubic susceptibility of Langmuir-Blodgette multilayers of polydiacetylene. *Thin Solid Films*, **132**, 11-19.

Kitchens, C. W., N. Gerber, and R. Sedney (1978) Spin decay of liquid-filled projectiles. *Journal of Spacecraft and Rockets*, **15**, 348-354.

Kitchens, C. W. Jr. (1980) Navier-Stokes solution for spin-up in a filled cylinder. *AIAA Journal*, **18**, 929-934.

Ledoux, I., D. Josse, P. Vidakovic, and J. Zyss (1986) Highly efficient single-crystalline organic thin film for quadratic nonlinear optics. *Optical Engineering*, **25**, 202-210.

Nayar, B. K. and C. S. Winter (1990) Organic second-order nonlinear optical materials and devices. *Optical and Quantum Electronics*, **22**, 297-318.

Paley, M. S., D. O. Frazier, H. Abeledeyem, S. P. McManus, and S. E. Zutant (1992) Synthesis, vapor growth, polymerization of thin films of novel diacetylene derivatives of pyrrole. The use of computer modeling to predict chemical and optical properties of these diacetylenes and polydiacetylenes. *J. American Chemical Society*, **114**, 3247-3251.

Seymour, R. J., G. M. Carter, Y. J. Chen, B. S. Elman, M. E. Rubner, M. K. Thakur, and S. K. Tripathy (1985) Polydiacetylene polymeric crystal for nonlinear optical applications. *SPIE Proceedings*, **567**, 56-60.

Thakur, M. and S. Meyler (1985) Growth of large-area thin-film single crystals of polydiacetylenes. *Macromolecules*, **18**, 2341-2344.

Thakur, M., G. M. Carter, S. Meyler, and H. Hryniewicz (1986) Growth and optical properties of thin film polydiacetylene single crystal. *Polymer Preprints*, **27**(1), 49-51.

# 斜向重力加速度影響下對流主導材料處理
# 之流體速度及溫度分佈

## 洪儒珍　　龍瀛天

美國阿拉巴馬大學機械與航空太空工程學系

## 摘　　要

在法向及斜向重力加速度影響下，熱對流在極低壓力下，由原始材料經蒸汽沈澱處理之數學模式作了研討：在法向重力加速度作用時，熱對流所推動的蒸汽沈澱可在複雜的回流流動模型下完成。在此種複雜的回流及非均勻溫度分佈的模型下，顯然無法達成處理均勻精細的結晶狀薄膜。在斜向作用時，重力加速度可分解成垂直減弱加速度及水平分量加速度。沿重力加速度垂直的剖面上可看出，減弱重力加速度可促進簡單向上流動及均勻溫度分佈。此種流體運動及均勻溫度分佈可形成有利造成良好光學材料之晶體成長的環境。但因有水平分量加速度的存在，總體上斜向重力加速度仍無法推動勻質晶體的成長。因此，要造成勻質晶體成長的環境，恐怕仍有賴於在微重力太空環境下，來推動晶體的成長。